Validation of 3D synthetic seismograms based on the ray-Born approximation

LIBOR ŠACHL

Department of Geophysics, Faculty of Mathematics and Physics, Charles University in Prague, V Holešovičkách 2, 180 00 Praha 8, Czech Republic (sachl@karel.troja.mff.cuni.cz)

Received: March 20, 2012; Revised: May 6, 2012; Accepted: July 10, 2012

ABSTRACT

The first-order Born approximation is a weak scattering perturbation method which is a powerful tool. The combination of the Born approximation and the ray theory enables to extend the applicability of the ray theory in terms of the required smoothness of the model and ensures faster computations than with, e.g., the finite difference method. We are motivated to describe and explain the effects of the numerical discretization of the Born integral on the resulting seismograms.

We focus on forward modelling and study the cases in which perturbation from the background model contains the interface. We restrict ourselves to isotropic models that contain two homogeneous layers. We compare the 2D and 3D ray-based Born-approximation seismograms with the ray-theory seismograms.

The Born seismograms are computed using a grid of finite extent. We anticipate that the computational grid should contain an appropriate number of gridpoints, otherwise the seismogram would be inaccurate. We also anticipate that the limited size of the computational grid can cause problems.

We demonstrate numerically that an incorrect grid can produce significant errors in the amplitude of the wave, or it can shift the seismogram in time. Moreover, the grid boundaries work as interfaces, where spurious waves can be generated. We also attempt to explain these phenomena theoretically. We give and test the options of removing the spurious waves. We show that it is possible to compute the Born approximation in a sparser grid, if we use elastic parameters averaged from some dense grid.

Keywords: Born approximation, ray theory, velocity model, perturbation

1. INTRODUCTION

In computing seismograms in a complex structure, we can meet a situation for which the method we are using is not suitable, or to which it cannot be even applied. A good example is the ray theory, which has certain advantages when compared with other methods, is not applicable if the medium is not smooth enough. A possible solution is to use a model which is close to the original one and satisfies the theory requirements. Let us call this model background and the original one perturbed. We know approximately the wavefield in the background model and wish to estimate the wavefield in the perturbed

Stud. Geophys. Geod., 57 (2013), 84–102, DOI: 10.1007/s11200-012-0722-5

model. It is possible to use the first-order Born approximation, which requires the quantities computed in the background model and differences between the perturbed and background model called perturbations. The result is a correction of the wavefield generated in the background model.

The Born approximation is a useful tool. *Moser (2012)* mentions its 3 important applications:

1. It can be used to test migration algorithms;
2. It can be used to study the effect of small perturbations of the existing model (scenario testing);
3. It can help in acquisition survey design.

Klimeš (2010, 2012a,b) deal with the aforementioned applications. The first-order Born approximation can be useful for the first mentioned application, because it generates idealized synthetic data, which contain primaries only (e.g., *Chauris et al., 2002*). According to *Jin et al. (1992)*, the important advantage of the ray-based Born modelling is computational efficiency. Another point in favour is that a general acquisition geometry and surface topography can be considered, as well as arbitrary locations of the scatterers in the model, with no restrictions to model topology (*Moser, 2012*).

As already mentioned, the Born approximation can be used for inversion algorithms, see, e.g., *Cohen et al. (1986)*, *Beydoun and Mendes (1989)* and *Thierry et al. (1999)*. *Thierry et al. (1999)* pointed out that the ray-based Born approach allows a great simplification in the migration algorithm thanks to low storage space of Green's functions computed by the ray theory.

Other papers focus on the Born approximation itself. *Coates and Chapman (1990)* studied the Born approximation in comparison with the ray perturbation theory. They restricted themselves to studying slowness perturbations (although the Born approximation is capable of dealing with perturbations of density and Lamé parameters). They considered the scattered signal from that part of the model that is near the reference ray and is well described by the first terms of a Taylor expansion of the model. They demonstrated the agreement, in the far field, of the two methods to the first order in the slowness perturbation and to the leading order in the asymptotic ray series. *Hudson and Heritage (1981)* attempted to define the cases within which the Born approximation may be regarded as reasonably accurate. They derived inequalities which govern the ranges of the parameters of the problem. These inequalities should help to asses the situation in which the Born approximation is not applicable. Correctness of the inequalities obtained is proved by comparison with the exact solution for a special case. The scattering of a plane wave by a homogeneous sphere with different properties than the surrounding homogeneous medium is treated. *Gibson and Ben-Menahem (1991)* analysed Rayleigh scattering using the Born approximation. They assumed an anisotropic obstacle embedded within an anisotropic matrix and showed that a perturbation of any of the 21 independent elastic parameters acts as a secondary moment tensor source which radiates energy as it is encountered by the incident wave. Further on, they studied the case of an anisotropic obstacle in an isotropic background medium in more detail and examined the case of a small fractured volume. *Ursin and Tygel (1997)* used ray-theory Green's functions from the source and receiver to the scattering point and assumed that the parameters of the medium vary slowly except along a surface, along which they vary considerably. They

applied these assumptions to derive reciprocal surface scattering integrals. *Beydoun and Tarantola (1988)* studied the pressure-field response from a one-dimensional velocity slab immersed in an infinite constant velocity medium. The analytical expressions are used for comparison with the results obtained by both the first Born and first Rytov approximations. They conclude that the first Born approximation is best suited for modelling and inverting the primary reflected, or backscattered part of the wavefield.

In this paper, we address the numerical realization of the Born seismogram computations. We are interested in the impact of the discretization of the Born integral on the accuracy of the Born seismograms, i.e. we are interested in the effects of a grid density, finite extent of the grid, etc.

The paper is organized as follows: The theory of the ray-based Born approximation is given in Section 2. Two models of our interest are presented in Section 3. The following Sections 4 and 5 are the key parts of the paper. The Born and ray-theory seismograms computed in the models of Section 3 are compared there, and the observed features are discussed. Section 4 is devoted to the 3D Born approximation, Section 5 is devoted to the 2D Born approximation. The paper is closed by remarks in Section 6.

The Einstein summation convention is used throughout this paper.

2. THE RAY-BASED BORN APPROXIMATION IN AN ISOTROPIC MEDIUM, WITH POINT-SOURCE AND HIGH-FREQUENCY APPROXIMATION

The first-order Born approximation reads (*Červený, 2001, Eq. 2.6.18*)

$$\begin{aligned}\Delta u_n(\mathbf{x},\omega) = \int_\Omega \Big[& \omega^2 u_i(\mathbf{x}',\omega)\Delta\rho(\mathbf{x}')G_{ni}(\mathbf{x},\mathbf{x}',\omega) \\ & - u_{k,l}(\mathbf{x}',\omega)\Delta c_{ijkl}(\mathbf{x}')G_{ni,j}(\mathbf{x},\mathbf{x}',\omega)\Big] d^3\mathbf{x}',\end{aligned} \tag{1}$$

where ω is the circular frequency, $\Delta c_{ijkl}(\boldsymbol{x}')$ and $\Delta\rho(\mathbf{x}')$ are the perturbations of elastic moduli and density, Ω is the domain where these perturbations are non-zero, $u_i(\mathbf{x}',\omega)$ is the solution of the elastodynamic equation for the background medium, $G_{ij}(\mathbf{x},\mathbf{x}',\omega)$ is the Green's function in the background medium and $G_{ij,k}(\mathbf{x},\mathbf{x}',\omega)$ is the spatial derivative of the Green's function with respect to x_k'. *Moser (2012)* points out that no special requirements regarding the smoothness of $\Delta\rho(\mathbf{x}')$ and $\Delta c_{ijkl}(\mathbf{x}')$ are necessary. We consider an isotropic medium. We insert the expression for the components of the elastic tensor in the isotropic solid into Eq (1) to obtain

$$\begin{aligned}\Delta u_i(\mathbf{x},\omega) = \int_\Omega \Big[& \omega^2 \Delta\rho(\mathbf{x}')G_{ij}(\mathbf{x},\mathbf{x}',\omega)u_j(\mathbf{x}',\omega) \\ & - \Delta\lambda(\mathbf{x}')G_{ij,j}(\mathbf{x},\mathbf{x}',\omega)u_{k,k}(\mathbf{x}',\omega) \\ & - \Delta\mu(\mathbf{x}')G_{ik,j}(\mathbf{x},\mathbf{x}',\omega)\big(u_{k,j}(\mathbf{x}',\omega)+u_{j,k}(\mathbf{x}',\omega)\big)\Big] d^3\mathbf{x}',\end{aligned} \tag{2}$$

where $G_{ij,k}(\mathbf{x},\mathbf{x}',\omega)$ is the spatial derivative of the Green's function with respect to x'_k. We assume that a point source is located at point $\mathbf{x}^s$. The wavefield and the Green's function in the background model are computed using the ray theory. Let us decompose the wavefield and the Green's function into amplitudes a_i, A_{ij} and phase terms $\exp(\mathrm{i}\omega\tau(\mathbf{x}'))$, $\exp(\mathrm{i}\omega T(\mathbf{x}'))$. We arrive at the ray-theory approximation

$$u_i(\mathbf{x}',\omega) = a_i(\mathbf{x}')\exp(\mathrm{i}\omega\tau(\mathbf{x}')), \tag{3}$$

$$G_{ij}(\mathbf{x},\mathbf{x}',\omega) = A_{ij}(\mathbf{x},\mathbf{x}')\exp(\mathrm{i}\omega T(\mathbf{x}')), \tag{4}$$

where $\tau(\mathbf{x}')$ is the travel time from $\mathbf{x}^s$ to $\mathbf{x}'$, i.e. from the point source to an integration point, and $T(\mathbf{x}')$ is the travel time from $\mathbf{x}'$ to $\mathbf{x}$, i.e. from an integration point to the receiver. We compute the travel time solving the eikonal equation; the amplitude is determined using dynamic ray tracing, see *Červený (2001)*.

We now apply the high-frequency approximation of the spatial derivatives,

$$u_{i,j}(\mathbf{x}',\omega) \approx \mathrm{i}\omega a_i(\mathbf{x}')\,p_j(\mathbf{x}')\exp(\mathrm{i}\omega\tau(\mathbf{x}')), \tag{5}$$

$$G_{ij,k}(\mathbf{x},\mathbf{x}',\omega) \approx \mathrm{i}\omega A_{ij}(\mathbf{x},\mathbf{x}')\,P_k(\mathbf{x}')\exp(\mathrm{i}\omega T(\mathbf{x}')), \tag{6}$$

where $p_i(\mathbf{x}')$ is the spatial derivative of travel time $\tau(\mathbf{x}')$ with respect to x'_i and $P_i(\mathbf{x}')$ is the spatial derivative of travel time $T(\mathbf{x}')$ with respect to x'_i. $G_{ij,k}(\mathbf{x},\mathbf{x}',\omega)$ is the spatial derivative of the Green's function with respect to x'_k.

Using Eqs (3)–(6), Eq. (2) becomes

$$\begin{aligned}\Delta u_i(\mathbf{x},\omega) = \omega^2 \int_\Omega \exp\left[\mathrm{i}\omega\left(\tau(\mathbf{x}')+T(\mathbf{x}')\right)\right] \\ \Big[\Delta\rho(\mathbf{x}')\,A_{ij}(\mathbf{x},\mathbf{x}')\,a_j(\mathbf{x}')+\Delta\lambda(\mathbf{x}')\,A_{ij}(\mathbf{x},\mathbf{x}')\,P_j(\mathbf{x}')\,a_k(\mathbf{x}')\,p_k(\mathbf{x}') \\ +\Delta\mu(\mathbf{x}')\,A_{ik}(\mathbf{x},\mathbf{x}')\,P_j(\mathbf{x}')\left(a_k(\mathbf{x}')\,p_j(\mathbf{x}')+a_j(\mathbf{x}')\,p_k(\mathbf{x}')\right)\Big]\,d^3\mathbf{x}'.\end{aligned} \tag{7}$$

If the source and receiver are situated in symmetry plane S of a 2D model, we can compute the Born approximation numerically in a 2D slice and perform the remaining one-dimensional integration analytically in the direction perpendicular to the slice, applying the method of stationary phase. We consider a Cartesian coordinate system with horizontal coordinate x_1, vertical coordinate x_3 and $x_2 = 0$ for all points in the slice. The equation in the acoustic medium is derived in *Červený and Coppoli (1992)*. The case of the elastic medium is treated in *Foss et al. (2005)* and *Bansal and Sen (2010)*; the resulting equation has the form

$$\Delta u_i(\mathbf{x},\omega) = \omega^2 \int_S \sqrt{\frac{\pi}{\omega\left(\tau_{,22}(\mathbf{x}') + T_{,22}(\mathbf{x}')\right)}}\,(1+\mathrm{i})\exp\left[\mathrm{i}\omega\left(\tau(\mathbf{x}') + T(\mathbf{x}')\right)\right]$$
$$\left[\Delta\rho(\mathbf{x}')\,A_{ij}(\mathbf{x},\mathbf{x}')\,a_j(\mathbf{x}') + \Delta\lambda(\mathbf{x}')\,A_{ij}(\mathbf{x},\mathbf{x}')\,P_j(\mathbf{x}')\,a_k(\mathbf{x}')\,p_k(\mathbf{x}')\right. \tag{8}$$
$$\left. + \Delta\mu(\mathbf{x}')\,A_{ik}(\mathbf{x},\mathbf{x}')\,P_j(\mathbf{x}')\left(a_k(\mathbf{x}')\,p_j(\mathbf{x}') + a_j(\mathbf{x}')\,p_k(\mathbf{x}')\right)\right] d^3\mathbf{x}',$$

where $\tau_{,22}(\mathbf{x}')$ and $T_{,22}(\mathbf{x}')$ are the second spatial derivatives of travel time $\tau(\mathbf{x}')$ and travel time $T(\mathbf{x}')$ in the direction of the x_2 axis at point $\mathbf{x}'$, respectively. Thus, we can compute the Born approximation in the same way as in a 3D model, the only modification being the multiplication of the integrand in the Born integral by term

$$I_{cor} = \sqrt{\frac{\pi}{\omega\left(\tau_{,22}(\mathbf{x}') + T_{,22}(\mathbf{x}')\right)}}\,(1+\mathrm{i}). \tag{9}$$

The validity of the ray-based Born approximation relies upon the validity of the Born approximation and the ray theory. The Born approximation requires the first-order scattered wave to be much smaller than the background wave. This condition can be satisfied using a low frequency or a small scatterer. On the other hand, if we construct a realistic background in order to obtain a small scatterer, the ray theory may be invalid (*Moser, 1997*). The ray theory requires the wavelength to be much smaller than the characteristic length of the background model. Additionally, the ray theory is not valid in caustics or in their vicinity (*Červený, 2001*).

3. MODELS

Coordinates x_1 and x_2 are the horizontal coordinates. Coordinate x_3 is the vertical coordinate. The x_3 coordinate axis is oriented downwards in both the background and perturbed models. The background model is homogeneous without interfaces. The values of the elastic parameters are

$$v_P = 6 \text{ km s}^{-1}, \quad v_S = 3 \text{ km s}^{-1}, \quad \rho = 2000 \text{ kg m}^{-3}.$$

Each perturbed model contains two homogeneous layers. The models differ in the shape of the interface between the layers and in the model volume. The values of the elastic parameters in the upper layer are equal to the values in the background model. The values of the elastic parameters in the lower layer are

$$v_P = 6.01 \text{ km s}^{-1}, \quad v_S = 3.01 \text{ km s}^{-1}, \quad \rho = 2010 \text{ kg m}^{-3}.$$

Model 1 has a horizontal interface at a depth of 10 km. The model volume is (0 km, 10 km) × (0 km, 10 km) × (0 km, 20 km). See Fig. 1.

Model 2 has a curved interface. The model volume is (−5 km, 15 km) × (0 km, 10 km) × (0 km, 20 km). See Fig. 2.

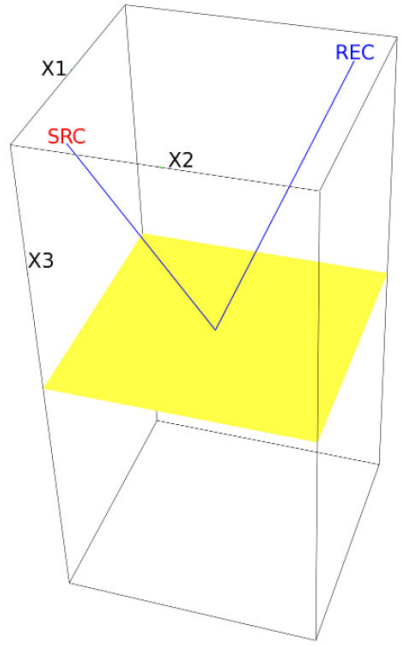

Fig. 1. The model volume, the interface and the reflected ray from source SRC to receiver REC in Model 1. The figure of the model was created in program GOCAD.

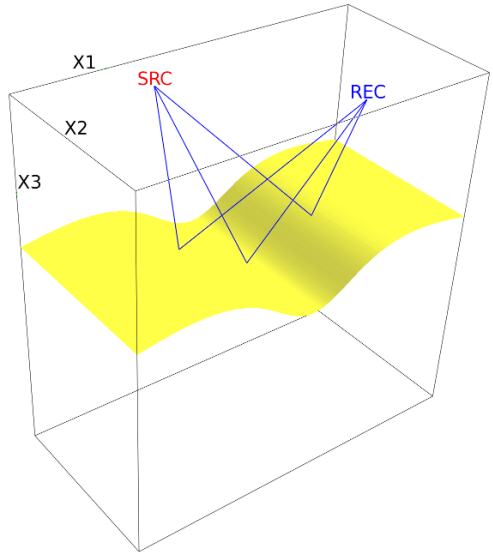

Fig. 2. The model volume, the interface and the reflected rays from source SRC to receiver REC in Model 2.

4. NUMERICAL EXAMPLES OF 3D COMPUTATIONS OF SEISMOGRAMS FOR 3D ELASTODYNAMIC EQUATION

The explosive source is situated at point (2 km, 1 km, 1 km), the receiver at point (8 km, 9 km, 0 km) in both models. The source time function is a Gabor signal with a prevailing frequency of 10 Hz, filtered by a frequency filter which is non-zero only for frequencies f, $1 < f < 20$ Hz. There is a cosine tapering for $1 < f < 2$ Hz and $19 < f < 20$ Hz while for $2 < f < 19$ Hz the filter is equal to one. We use a frequency filter to have the non-zero source time function only in a finite frequency interval and also to avoid low frequencies. Just P-waves are considered in all numerical examples except for one numerical example focused on S waves.

We note the grid intervals of the computational grid in the directions of the x_1, x_2, x_3 coordinate axes by D_1, D_2, D_3, respectively.

4.1. Model 1

4.1.1. Model 1 - grid density

The position of the grid with respect to the horizontal interface is depicted in Fig. 3. The interface is situated precisely between two gridpoint planes. The distance between the model boundary and the nearest gridpoint plane is equal to half the grid interval, because the value of any quantity at each gridpoint represents the value in the block centred at the gridpoint with sides equal to the grid intervals.

For the position of the coordinate axes, refer to Fig. 1 in Section 3. We start with Grid 1, see Table 1. Grid 1 covers only the lower part of the model, where the perturbation is non-zero in order to save memory. The grid interval is taken to be 0.1 km, which is smaller than a quarter of the wavelength, $\lambda/4 = 0.15$ km, where we have used $\lambda = v_P / f_d$ with the prevailing frequency of the Gabor signal $f_d = 10$ Hz and P-wave velocity $v_P = 6$ km s^{-1}.

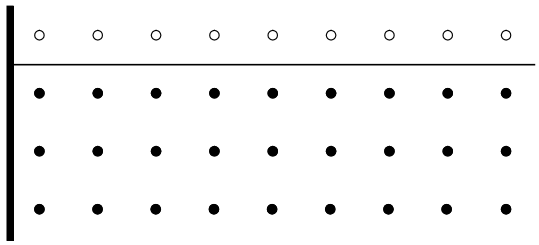

Fig. 3. Position of the grid in Model 1, which discretizes the interface in the best way. Bold line: Model boundary. Thin line: Interface. The white circles represent the gridpoints where perturbations are zero.

Table 1. Grids used in computations in Model 1.

Grid Number	Domain Covered by the Grid (values in km)	Number of Gridpoints
1	(0, 10) × (0, 10) × (10, 20)	100 × 100 × 100
2	(0, 10) × (0, 10) × (10, 20)	100 × 100 × 200
3	(0, 10) × (0, 10) × (10, 20)	200 × 100 × 200
4	(0, 10) × (0, 10) × (10, 20)	100 × 100 × 400
5	(0.2, 9.8) × (0.2, 9.8) × (10, 19.8)	96 × 96 × 392
6	(−10, 20) × (−10, 20) × (10, 20)	300 × 300 × 400
7	(−10, 20) × (−10, 20) × (10, 20)	75 × 75 × 400
8	(0, 10) × (0, 10) × (10, 20)	100 × 100 × 800

The result is the blue seismogram in Fig. 4. We can see that the main features have been accounted for, but obviously some discrepancies are present. The discrepancies are caused by the too coarse grid used. We densify Grid 1 in order to prove this statement. First, we use Grid 2, which is densified twice in the direction of the third axis. The resulting green seismogram in Fig. 4 is better than the previous one. We then use Grid 3, which corresponds to Grid 2 additionally densified in the direction of the first axis. It is slightly surprising that this has no impact on the seismogram. Therefore, we go back and use Grid 4, which corresponds to Grid 2 additionally densified in the direction of the third axis. The seismogram has improved, see the red seismogram in Fig. 4. There are virtually no differences between the Born and ray-theory seismogram.

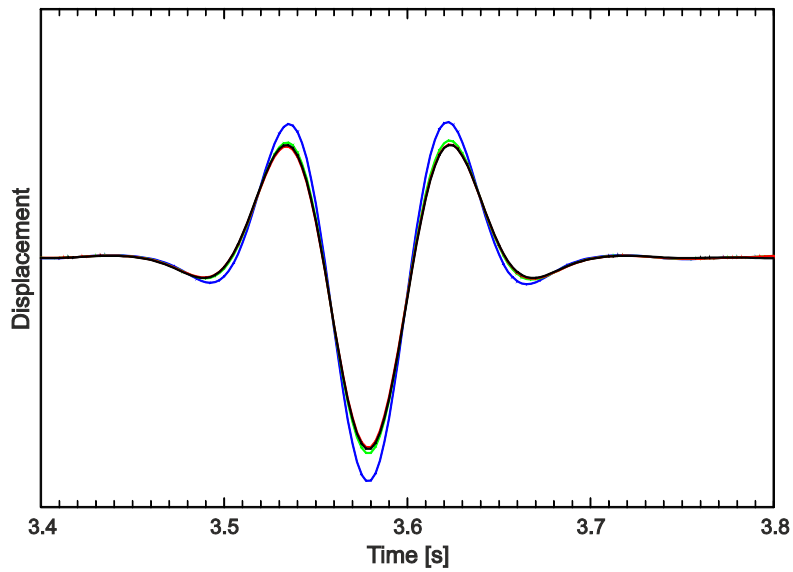

Fig. 4. Born (blue, green, red) and ray-theory (black) seismograms computed in Model 1. The Born seismograms are computed using Grid 1 (blue), Grid 2 (green) and Grid 4 (red). The seismograms are plotted in color order blue, green, red, black.

We try to understand the effect of discretization. Let us assume the paraxial approximation with the first-order Taylor expansion of travel time with respect to the spatial coordinates. The central point is the point of reflection, therefore, the derivatives of travel time with respect to the first and second coordinate axes are equal to zero, and the integral in the Born approximation in the homogeneous model can be simplified to

$$I_0 = \int_0^\infty \exp\left(\mathrm{i}\omega\hat{p}_3 x_3\right) \mathrm{d}x_3 = -\frac{1}{\mathrm{i}\omega\hat{p}_3}, \tag{10}$$

where

$$\omega = \frac{2\pi v}{\lambda}, \qquad \hat{p}_3 = p_3 + P_3 = \frac{2\cos\alpha}{v}, \tag{11}$$

α being the angle between the slowness vector of the incident wave and the normal to the interface. Discretization with the grid interval h affects the integral in the following way:

$$I_1 = \sum_{n=0}^{\infty} h \exp\left[\mathrm{i}\omega\hat{p}_3\left(\frac{h}{2}+nh\right)\right] = h\exp\left(i\omega\hat{p}_3\frac{h}{2}\right)\frac{1}{1-\exp\left(\mathrm{i}\omega\hat{p}_3 h\right)}. \tag{12}$$

Equations (10) and (12) yield

$$\frac{I_1}{I_0} - 1 = -\mathrm{i}\omega\hat{p}_3 h \frac{\exp\left[\mathrm{i}\omega\hat{p}_3\left(h/2\right)\right]}{1-\exp\left(\mathrm{i}\omega\hat{p}_3 h\right)} - 1 = \frac{\omega\hat{p}_3\left(h/2\right)}{\sin\left[\omega\hat{p}_3\left(h/2\right)\right]} - 1. \tag{13}$$

The expression in Eq. (13) is real and, therefore, the discretization error influences the amplitude of the wave, but not the phase. Equation (13) using Eq. (11) becomes

$$\frac{I_1}{I_0} - 1 = \frac{2\pi\left(h/\lambda\right)\cos\alpha}{\sin\left[2\pi\left(h/\lambda\right)\cos\alpha\right]} - 1, \tag{14}$$

which approximates to

$$\frac{I_1}{I_0} - 1 \approx \frac{1}{6}\left(2\pi\frac{h}{\lambda}\cos\alpha\right)^2. \tag{15}$$

The importance of approximate Eq. (15) is that it shows the proportionality of the error to $h^2\left(\cos^2\alpha\right)\big/\lambda^2$. We compare the numerical results with theoretical predictions given by Eqs (14) and (15), see Table 2. Both theoretical predictions (Eqs (14) and (15)) agree well with the numerical modelling in case of the smallest grid interval $D_3 = 0.025$ km in Grid 4. The differences between the theoretical predictions and numerical results are observed for $D_3 = 0.05$ km in Grid 2 and $D_3 = 0.1$ km in Grid 1. The difference between the full formula (15) and its first approximation (14) is negligible within our numerical

Table 2. Effect of the discretization error on the wave amplitude. Comparison of the theoretical prediction and the numerical results. D_3 is the grid interval in the direction of the third coordinate axis.

$h = D_3$ [km]	Eq. (15) [%]	Eq. (14) [%]	Measured [%]
0.1	14	16	17
0.05	3.6	3.7	2.2
0.025	0.9	0.9	0.9

accuracy for $D_3 = 0.025$ km. The difference grows for $D_3 = 0.05$ km and is important for $D_3 = 0.1$ km.

4.1.2. Model 1 - spurious waves

Unfortunately, the seismogram is still incorrect, see the red seismogram in Fig. 5, which is identical to the red seismogram in Fig. 4 with the time window extended from 3.4–3.8 s to 3.0–7.2 s. The differences are caused by interfaces artificially introduced by the grid. The model is defined within the model volume, but it smoothly continues across the model boundaries. Therefore, the model boundaries (side boundaries, bottom and top boundary) are not interfaces. However, our choice of the grid is equivalent to putting model perturbations zero elsewhere. In the case of Model 1, the boundaries of the lower part of the model are treated as interfaces. Consequently, the wave reflected from the bottom grid boundary, as well as diffractions, are visible in the red seismogram in Fig. 5; read the following text.

The spurious waves should change their position in the seismogram if we shift the grid boundaries. Consider α to be the angle between the normal to the interface and the vector tangent to the ray. The wave has to travel $\Delta l = d\cos\alpha$ more/less if we shift the grid boundary by d. We erase 2 side gridpoint planes and 8 bottom gridpoint planes in Grid 4, which results in Grid 5 and $d = -0.2$ km. The corresponding value of $|\Delta l| = 0.2\cos\alpha$ km is larger than $\lambda/4$ for normal incidence, but due to the cosine modification for oblique incidence, a larger value is better than smaller. The seismogram is displayed in Fig. 5 as the green seismogram.

The waves which are shifted in the seismogram should be eliminated. There are at least two ways of doing this. The first one is safe but expensive. It consists in a sufficient extension of the grid. If the grid boundaries (interfaces) are far enough, reflections, etc. arrive sufficiently late. The blue seismogram depicted in Fig. 5 is computed using Grid 6. Grid intervals in Grid 6 and Grid 4, which was used in computing the red seismograms in Figs 4 and 5, are the same but Grid 6 contains 9 times more gridpoints than Grid 4. Compare the four waves visible in the seismograms in Fig. 5. These four waves arrive at approximately 3.6 s, 3.9 s, 6.7 s and 6.9 s in the red Born seismogram. The first wave is obviously the true wave which is reflected from the model interface, because we see no shift in the green seismogram. The third wave is shifted in the green seismogram, but it is not shifted in the blue seismogram. We enlarge the model in the horizontal direction,

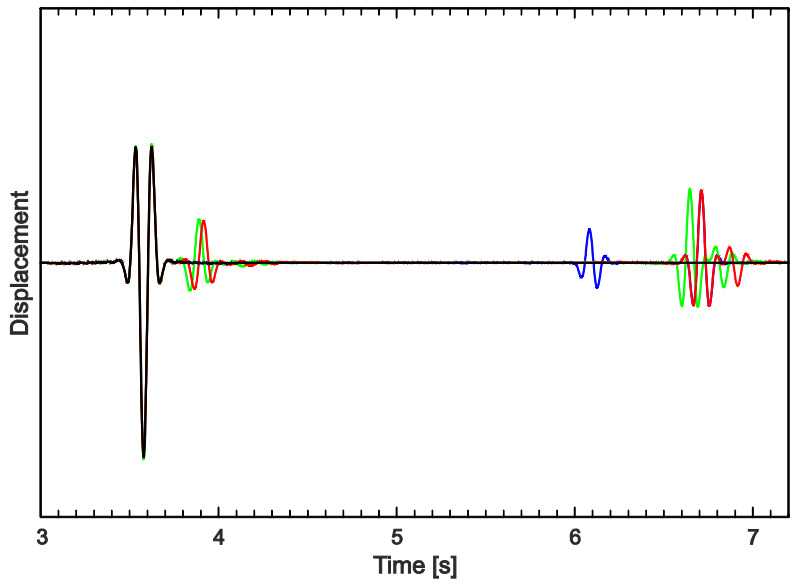

Fig. 5. Born (red, green, blue) and ray-theory (black) seismograms computed in Model 1. The Born seismograms are computed using Grid 4 (red), Grid 5 (green) and Grid 6 (blue). The four best visible waves in the red Born seismogram arrive at approximately 3.6 s, 3.9 s, 6.7 s and 6.9 s. The first wave in all three Born seismograms is obscured by the black ray-theory seismogram. The third wave in the blue Born seismogram is obscured by the red seismogram. The second wave in the blue Born seismogram is changed considerably and delayed. The fourth wave in the blue Born seismogram is not visible.

which means that the third wave is the reflection from the bottom grid boundary. The second wave is considerably changed and delayed in the blue seismogram; this is probably the diffraction at the intersection of the model interface with the grid boundary. The fourth wave is no longer visible in the blue seismogram; it could be a diffraction from the bottom grid edges. We have thus successfully delayed the waves from the side grid boundaries with the use of Grid 6.

One might think that we can use a sparser grid if we are sufficiently far from the source and the receiver. If this were true, we would be able to cover a large volume with only slightly more effort using varying grid density. Unfortunately, if we use dense Grid 4 in (0 km, 10 km) × (0 km, 10 km) × (10 km, 20 km) and sparse Grid 7 elsewhere in (−10 km, 20 km) × (−10 km, 20 km) × (10 km, 20 km), the resulting seismogram is incorrect. We observe strong spurious oscillations, which are the results of constructive interferences.

The second way of eliminating a spurious wave is to apply the cosine window at the artificial grid boundaries. The 1D cosine window starting at point x_s of length L is function

$$w(x)=\begin{cases} 0 & \text{for} \quad x < x_S\,, \\ \dfrac{1}{2}\left[1-\cos\dfrac{\pi(x-x_S)}{L}\right] & \text{for} \quad x \in \langle x_S,\, x_S+L\rangle, \\ 1 & \text{for} \quad x > x_S+L\,. \end{cases} \tag{16}$$

We introduce the numbering of the grid boundaries, see Table 3.

If we apply the cosine windows of length L to the 1st boundary at $\left(x_1^0, \bullet, \bullet\right)$, then the cosine window is function $w(x_1)$ defined by Eq. (16) with $x_S = x_1^0 - (D_1/2)$. Similarly for the other boundaries.

We apply the cosine windows of equal length to each grid boundary except the 5th, where we model the reflection. The tested lengths are L = 1, 1.5, 2, 2.5 and 3 km. Only the seismograms corresponding to L = 1, 1.5, and 2.5 km are displayed, see Fig. 6.

Notice that the amplitudes of the spurious waves decrease and the waves arrive earlier. The value of L = 2.5 km (and also L = 3 km) is too large; the spurious wave arrives so early that it interferes with the true wave. Another important fact is that the reflection from the bottom grid boundary is damped very well, while the diffractions from the side grid boundaries are damped less.

This phenomenon can be explained similarly as we derived Eq. (15). The Born approximation with the applied cosine window can be reduced to

$$I_1 = \int_0^L w(x)\exp\left(\mathrm{i}\omega\hat{p}_3 x_3\right) dx_3 + \int_L^\infty \exp\left(\mathrm{i}\omega\hat{p}_3 x_3\right) dx_3\,, \tag{17}$$

which, after some computation, yields

$$I_1 = \frac{(1/2)(\pi/L)^2}{\mathrm{i}\omega\hat{p}_3\left[(\omega\hat{p}_3)^2-(\pi/L)^2\right]}\left[1+\exp\left(\mathrm{i}\omega\hat{p}_3 L\right)\right]. \tag{18}$$

Table 3. Numbering of the grid boundaries.

Axis perpendicular to the boundary	Assigned number
1st, negative direction	1
1st, positive direction	2
2nd, negative direction	3
2nd, positive direction	4
3rd, negative direction	5
3rd, positive direction	6

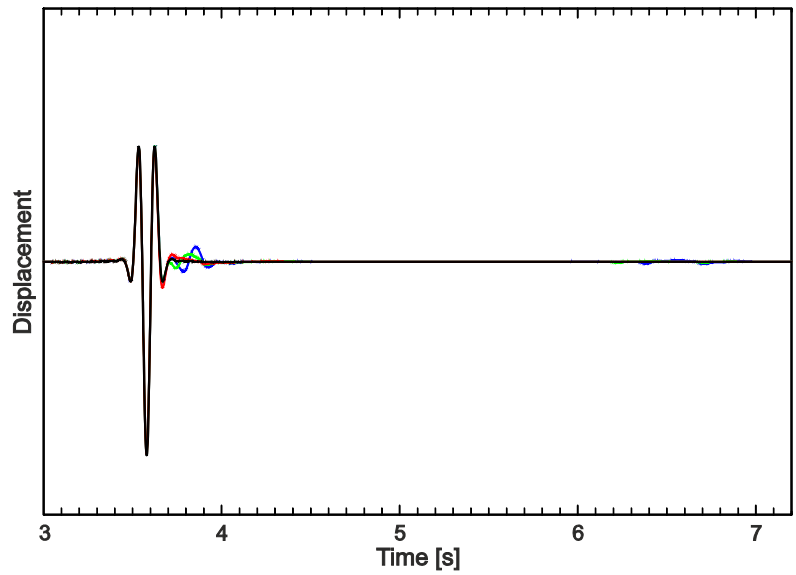

Fig. 6. Born (blue, green, red) and ray-theory (black) seismograms computed in Model 1. The Born seismograms are computed using Grid 4 with cosine windows 1 km (blue), 1.5 km (green) and 2.5 km (red) in length applied to grid boundaries 1, 2, 3, 4, 6. The Born seismograms are for the most part obscured by the ray-theory seismogram.

Using Eqs (10) and (18) we can put

$$\frac{I_1}{I_0} = \frac{(\pi/L)^2}{(\pi/L)^2 - (\omega \hat{p}_3)^2} \frac{1 + \exp(\mathrm{i}\omega \hat{p}_3 L)}{2}. \tag{19}$$

If we assume that $\omega \hat{p}_3 L \gg \pi$,

$$\left|\frac{I_1}{I_0}\right| < \left(\frac{\pi}{\omega \hat{p}_3 L}\right)^2, \tag{20}$$

and, employing Eq. (11), we arrive at

$$\left|\frac{I_1}{I_0}\right| < \left(\frac{\lambda}{4L\cos\alpha}\right)^2. \tag{21}$$

Equation (21) indicates that the damping of the spurious wave depends on $\lambda^2 / \left(L^2 \cos^2 \alpha\right)$. Therefore, we could have a serious problem with the wave that is incident nearly tangent to the interface.

4.1.3. Model 1 - other types of waves

Now we shall focus on other possible situations, i.e. the incident P wave and scattered S wave (P-S for short), S-P and S-S. We use Grid 4 in case of P-S, S-P and obtain seismograms which are in good agreement with the ray-theory seismograms. We also compute S-S seismograms with the use of Grid 4, but we observe some discrepancies. It is necessary to realize that $v_P = 6$ km s^{-1}, $v_S = 3$ km s^{-1} and thus $\lambda_S = \lambda_P/2$. Therefore, the grid should be twice denser to be effectively the same as in the case of P waves. If we employ Grid 8, which is twice denser in the vertical direction than Grid 4, the discrepancies disappear.

4.2. Model 2

For the position of the coordinate axes, refer to Fig. 2 in Section 3. We choose Grid 9 for the computations, see Table 4. Grid 9 contains only 100 gridpoints in the direction of the second coordinate axis, because the shape of the interface does not depend on x_2. The resulting green seismogram in Fig. 7 is satisfactory for lower arrival times, say until 3.4 s. But there is evidently something wrong with the waves which arrive later. We think that this is caused by the spurious waves diffracted from the intersection between the grid boundary perpendicular to the second coordinate axis and the interface. The computation using Grid 10 supports the idea. Grid 10 is smaller than Grid 9 in the direction of the second coordinate axis, i.e. we shift the grid boundary perpendicular to the second coordinate axis. The shift is equal to 0.2 km, i.e. approximately $\lambda/4$ similarly as in Section 4.1.2. We obtain the blue seismogram in Fig. 7. The first wave in the blue seismogram is unaffected, while the second wavegroup is shifted. The wavegroup is distorted, which means that the wavegroup is a superposition of 2 waves. One wave shifts and the other wave does not. The reflected wave is mixed with the numerically diffracted wave.

We follow the procedure from Section 4.1.2 and apply cosine window $L = 1.5$ km in length in the direction of the second coordinate axis. The obtained red seismogram in Fig. 7 depicts the good agreement between the Born and ray-theory seismograms.

Grid 9 is quite large. It would be useful, if we could save some time and get good results. We try to compute the Born approximation using Grid 11, which contains almost 4.5 times less gridpoints than Grid 9, but with more precise grid values of the elastic parameters. We discretize the density, P-wave and S-wave velocity in the grid twice denser in the direction of the first and third axes than Grid 11. The quantities are then averaged to Grid 11. The density is averaged by taking its geometrical mean, which corresponds to the conservation of mass inside the volume determined by the averaged

Table 4. Grids used in computations in Model 2.

Grid Number	Domain Covered by the Grid (values in km)	Number of Gridpoints
9	whole volume of Model 2	666 × 100 × 3200
10	(−5, 15) × (0.2, 9.8) × (0, 20)	666 × 96 × 3200
11	whole volume of Model 2	600 × 100 × 800

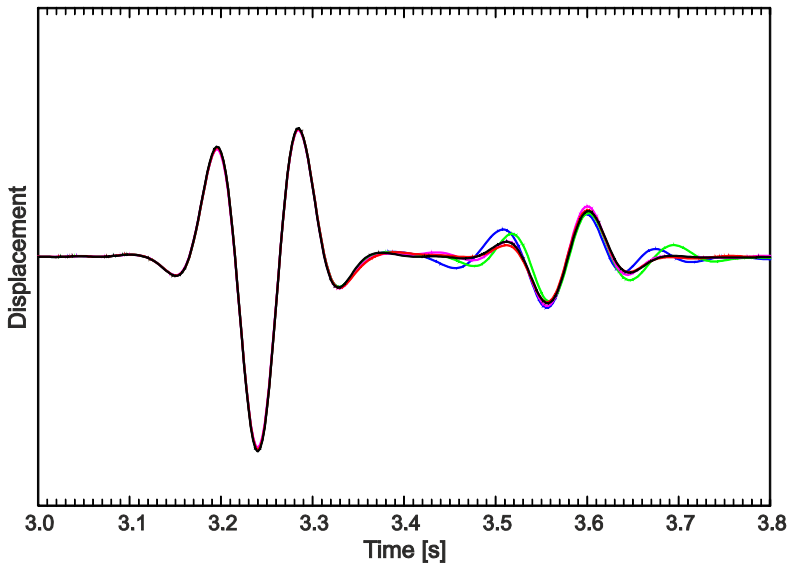

Fig. 7. Born (red, green, blue, pink) and ray-theory (black) seismograms computed in Model 2. The red and green Born seismograms are computed using Grid 9. The cosine window 1.5 km in length is applied to grid boundaries 3, 4 in the red seismogram; no cosine window is applied in the green seismogram. The blue Born seismogram is computed using Grid 10; no cosine window is applied. The pink Born seismogram is computed using Grid 11 with the averaged elastic parameters (see the text); the cosine window 1.5 km in length is applied to grid boundaries 3, 4. The red and pink Born seismograms are mostly obscured by the ray-theory seismogram.

grid cell. The P-wave and S-wave velocities are averaged by taking their harmonic mean, which corresponds to the conservation of travel time inside the volume determined by the averaged grid cell. The resulting pink Born seismogram in Fig. 7 corresponds a bit worse to the ray-theory seismogram than the red Born seismogram, but the coincidence is still satisfactory.

5. NUMERICAL EXAMPLES OF 2D COMPUTATIONS OF SEISMOGRAMS FOR 3D ELASTODYNAMIC EQUATION

Models 1 and 2 are exactly the same as those used in the 3D computations of Section 4 and are described in Section 3, but the source and the receiver positions are different. We have moved the source and the receiver into the symmetry plane. Namely the explosive source is at point (1.5 km, 5 km, 1 km) and the receiver at point (8.5 km, 5 km, 0 km).

5.1. Model 1

Using the experience from the 3D computations in Model 1, we start directly with Grid 12, see Table 5. The red seismogram displayed in Fig. 8 shows good agreement with the reference solution. It is interesting that the Born seismogram which is computed

Table 5. Grids used in 2D computations.

Grid Number	Domain Covered by the Grid (values in km)	Number of Gridpoints
12	(0, 10) × (10, 20)	100 × 400
13	(−5, 15) × (0, 20)	600 × 3200
14	(−5, 15) × (0, 20)	600 × 800

without correction given by Eq. (9) has an approximately 100 times larger amplitude than the ray-theory seismogram.

We try to demonstrate the importance of an appropriate discretization of the model interface by shifting the whole Grid 12 downwards. The shift is smaller than $D_3/2$ but it is close to this value. Fig. 8 shows that the blue Born seismogram is shifted in time with respect to the ray-theory seismogram. The shift is unwanted but the behaviour is correct. The interface is discretized between two gridpoint planes. We shift these planes downwards, so that the Born approximation shifts the interface downwards and the wave thus arrives later.

5.2. Model 2

Motivated by the computations in Section 4.2, we choose Grid 13, see Table 5. The calculated Born seismogram corresponds very well to the ray-theory seismogram, see the red seismogram in Fig. 9.

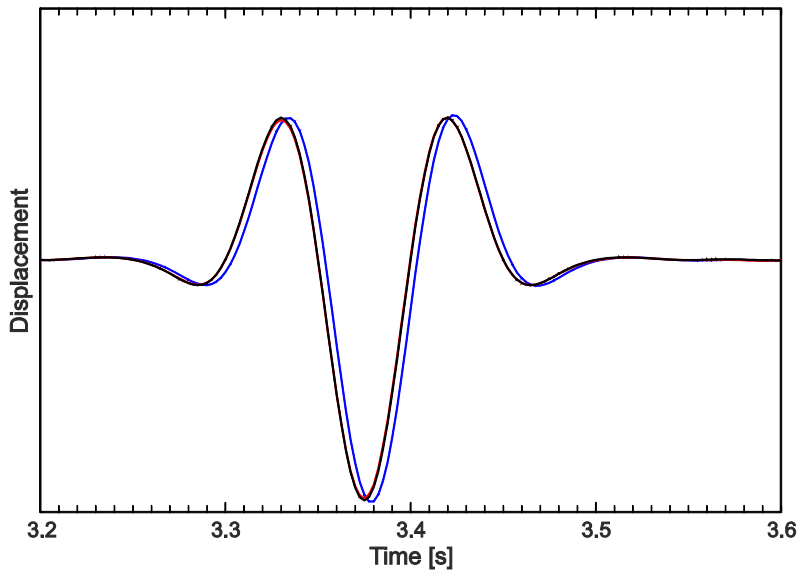

Fig. 8. Born (red, blue) and ray-theory (black) seismograms computed in Model 1. The Born seismograms are computed using the 2D Born approximation in Grid 12. The grid is slightly shifted downwards in computing the blue Born seismogram. The red Born seismogram is mostly obscured by the ray-theory seismogram.

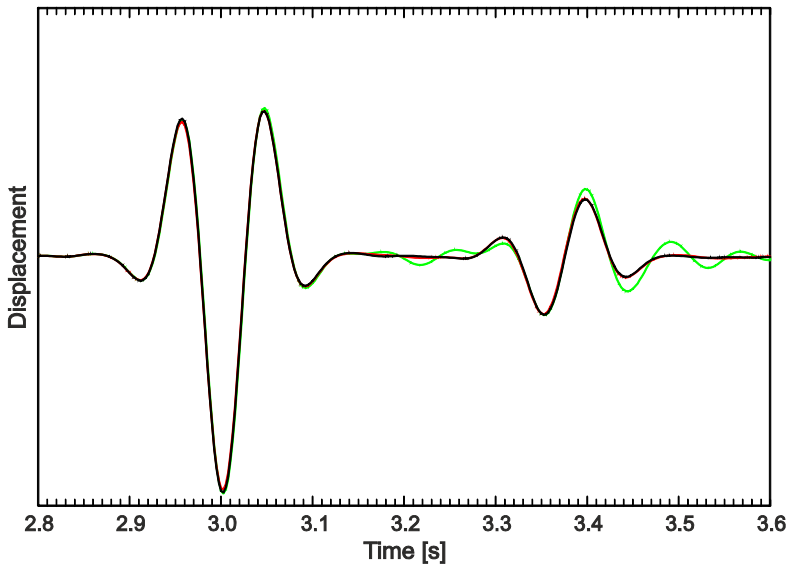

Fig. 9. Born (red, green) and ray-theory (black) seismograms computed in Model 2. The red and green Born seismograms are computed using the 2D Born approximation in Grid 13 and Grid 14, respectively. The red Born seismogram and the first wave in the green Born seismogram are mostly obscured by the ray-theory seismogram.

In the 2D computation, there is no grid boundary perpendicular to the second coordinate axis thanks to the numerical method used (analytical integration in the direction of the second coordinate axis). Remember that using an analogous grid in the 3D computation in Section 4.2, the Born and ray-theory seismograms did not agree until we applied cosine window $L = 1.5$ km in length in the direction of the second coordinate axis.

We also try Grid 14, which contains 4 times less gridpoints in the vertical direction than Grid 13. The resulting green seismogram is depicted in Fig. 9. It is interesting that the first wave is already well resolved using Grid 14, while there are apparent erroneous oscillations in the second wave.

6. CONCLUDING REMARKS

We have tested the ray-based first-order Born approximation in models with homogeneous background. We have proved that the Born integral has to be discretized using an appropriate grid, otherwise discrepancies and spurious waves occur. We have namely addressed the following issues:

- The grid has to be sufficiently dense, otherwise significant errors in the amplitude of the wave can be produced. The sufficient grid interval can be different in the direction of each coordinate axis. The smallest and largest grid intervals used in the successful computation was equal to $0.00625\,\text{km} = (1/96)\,\lambda \approx 0.01\,\lambda$ and

$0.1\,\mathrm{km} = (1/6)\lambda \approx 0.17\lambda$, respectively, where λ is the wavelength. We have derived an approximate formula, which estimates the magnitude of the error by $h^2\left(\cos^2\alpha\right)\big/\lambda^2$, where h is the grid interval perpendicular to the interface, λ is the wavelength and α is the angle between the slowness vector of the incident wave and the normal to the interface. The grid may be dense enough to resolve only a part of the seismogram if, e.g., the interface is curved strongly.

- It is not enough to have a sufficiently dense grid. The grid has to discretize the interface correctly too. The interface has to be located between two gridpoint planes otherwise the discretization shifts the interface. The Born seismogram is then shifted in time.
- Every computational grid has a finite extent. Spurious waves, which are either reflections or diffractions from the grid boundaries, can devalue the seismogram. The spurious waves can be clearly visible in the seismogram or they can be mixed with the true waves. We suggest shifting the grid boundaries slightly in order to detect the spurious waves. We propose 2 methods to remove the spurious waves:

  1. Enlarge the computational volume. Delayed spurious waves do not appear in the seismogram. This method is safe but expensive. We do not recommend enlarging the grid extent by using a sparse grid. The use of sparse instead of dense grid makes the method cheaper but it has not proved to be successful.
  2. Apply cosine window of the appropriate length to the integrand of the Born integral. The cosine window suppresses the spurious waves. The length of cosine window equal to 2.5λ seems to be recommendable but it is not universal. We have derived a formula, which indicates that the relative amplitude of the damped spurious wave, reflected from the grid boundary, depends on the angle of incidence considerably. If the angle of incidence is large, the damping of the spurious wave by applying the cosine window could be problematic.

We have not met any further problems in computing P-S, S-P and S-S Born seismograms.

It is possible to use a sparser grid with averaged elastic parameters to save time. Elastic parameters are first discretized in a dense grid and then averaged to a sparser grid.

We have also tested the 2D Born approximation with very good results. It seems that the 2D Born approximation requires a grid density similar to that of the 3D Born approximation.

Acknowledgements: First of all I would like to thank Luděk Klimeš, who helped me greatly with the work which led to this paper. I would also like to thank Václav Bucha who helped me with the figures of the models in Section 3. I am indebted to Ivan Pšenčík and Colin Thomson for helpful suggestions, and to two reviewers for constructive and useful reviews. The research has been supported by Charles University in Prague through Grant SVV-2012-265308, by the Czech Science Foundation under Contract P210/10/0736, by the Ministry of Education, Youth and Sports of the Czech Republic within Research Project MSM0021620860, and by members of the consortium "Seismic Waves in Complex 3-D Structures" (see *http://sw3d.cz*).

References

Bansal R. and Sen M.K., 2010. Ray-Born inversion for fracture parameters. *Geophys. J. Int.*, **180**, 1274–1288.

Beydoun W.B. and Mendes M., 1989. Elastic ray-Born l_2-migration/inversion. *Geophys. J. Int.*, **97**, 151–160.

Beydoun W.B. and Tarantola A., 1988. First Born and Rytov approximations: Modeling and inversion conditions in a canonical example. *J. Acoust. Soc. Am.*, **83**, 1045–1055.

Chauris H., Noble M.S., Lambaré G. and Podvin P., 2002. Migration velocity analysis from locally coherent events in 2-D laterally heterogeneous media. Part II: Applications on synthetic and real data. *Geophysics*, **67**, 1213–1224.

Coates R.T. and Chapman C.H., 1990. Ray perturbation theory and the Born approximation. *Geophys. J. Int.*, **100**, 379–392.

Cohen J.K., Hagin F.G. and Bleistein N., 1986. Three-dimensional Born inversion with an arbitrary reference. *Geophysics*, **51**, 1552–1558.

Červený V. and Coppoli A.D.M., 1992. Ray-Born synthetic seismograms for complex structures containing scatterers. *J. Seism. Explor.*, **1**, 191–206.

Červený V., 2001. *Seismic Ray Theory*. Cambridge Univ. Press., Cambridge, U.K.

Foss S.-K., de Hoop M.V. and Ursin B., 2005. Linearized 2.5-dimensional parameter imaging inversion in anisotropic elastic media. *Geophys. J. Int.*, **161**, 722–738.

Gibson R.L. and Ben-Menahem A., 1991. Elastic wave scattering by anisotropic obstacles: Application to fractured volumes. *J. Geophys. Res.*, **96**, 19905–19924.

Hudson J.A.. and Heritage J.R., 1981. The use of the Born approximation in seismic scattering problems. *Geophys. J. R. Astr. Soc.*, **66**, 221–240.

Jin S., Madariaga R., Virieux J. and Lambaré G., 1992. 2-dimensional asymptotic iterative elastic inversion. *Geophys. J. Int.*, **108**, 575–588.

Klimeš L., 2010. Sensitivity Gaussian packets. *SEG Expanded Abstracts*, **29**, 2779–2783.

Klimeš L., 2012a. Resolution of prestack depth migration. *Stud. Geophys. Geod.*, **56**, 457–482.

Klimeš L., 2012b. Sensitivity of seismic waves to structure. *Stud. Geophys. Geod.*, **56**, 483–520.

Moser T.J., 1997. Influence of realistic backgrounds on the validity and performance of ray/Born inversion. *J. Seism. Explor.*, **6**, 239–252.

Moser T.J., 2012. Review of ray-Born forward modeling for migration and diffraction analysis. *Stud. Geophys. Geod.*, **56**, 441–432.

Thierry P., Operto S. and Lambaré G., 1999. Fast 2-D ray+Born migration/inversion in complex media. *Geophysics*, **64**, 162–181.

Ursin B. and Tygel M., 1997. Reciprocal volume and surface scattering integrals for anisotropic elastic media. *Wave Motion*, **26**, 31–42.